

Microscopic Observation of Pauli Blocking in Degenerate Fermionic Lattice Gases

Ahmed Omran,^{1,*} Martin Boll,¹ Timon Hilker,¹ Katharina Kleinlein,¹
Guillaume Salomon,¹ Immanuel Bloch,^{1,2} and Christian Gross¹

¹*Max-Planck-Institut für Quantenoptik, 85748 Garching, Germany*

²*Ludwig-Maximilians-Universität, Fakultät für Physik, 80799 München, Germany*

The Pauli exclusion principle is one of the most fundamental manifestations of quantum statistics. Here, we report on its local observation in a spin-polarized degenerate gas of fermions in an optical lattice. We probe the gas with single-site resolution using a new generation quantum gas microscope avoiding the common problem of light induced losses. In the band insulating regime, we measure a strong local suppression of particle number fluctuations and a low local entropy per atom. Our work opens a new avenue for studying quantum correlations in fermionic quantum matter both in and out of equilibrium.

Quantum statistics distinguishes between two fundamentally different kinds of particles: bosons, which condense into a single quantum state at zero temperature, and fermions, for which multiple occupancy of a single state is forbidden. As a result, identical fermions seem to repel each other, described by an effective Fermi pressure on a macroscopic level [1]. Microscopically, the Pauli blockade manifests itself in a strong suppression of density fluctuations [2, 3] and in antibunching of density-density correlations [4–9]. Specifically, fermions in periodic potentials form a band insulating state with suppressed number fluctuations on each site when the chemical potential lies in the band gap. Measuring these number fluctuations can therefore be regarded as a direct probe of Pauli blocking.

Local fluctuations in periodic potentials have been directly studied with ultracold bosonic atoms in optical lattices [10–12]. Some of these experiments featured site-resolved fluorescence detection with single atom sensitivity [13, 14], which has proven to be a powerful method for probing quantum many-body systems. However, such quantum gas microscopy requires a specialized experimental setup with considerably increased technical complexity. In particular, the often used fermionic alkali atoms are difficult to laser cool, making the single-site and atom resolved detection even more challenging. First results have recently been reported on the imaging of single fermions in dilute thermal clouds [15–18]. However, microscopy of quantum degenerate fermions has so far remained out of reach.

Here, we report on the site-resolved characterization of a spin-polarized degenerate Fermi gas in an optical lattice. In the band-insulating region, we measure a strong suppression of local atom number fluctuations, more than one order of magnitude below the Poisson limit expected for uncorrelated particles. Based on the measurement of the local occupation statistics, we reconstruct the spatial entropy distribution in the inhomogeneous samples. We obtained these results with a conceptionally novel quantum gas microscope based on an additional, dedicated optical lattice for detection. This provides high flexibil-

ity for future experiments and offers an alternative approach [19, 20] to overcome the limitations due to parity detection [12, 14].

Our experiments started in a standard magneto-optical trap of ${}^6\text{Li}$ loaded from a Zeeman slower (for details see supplemental material). We further cooled the atoms using narrow-line laser cooling on the 323 nm line [21, 22]. The resulting 50/50 spin mixture of fermions in the $|F, m_F\rangle = |1/2, \pm 1/2\rangle$ states was then loaded into an optical trap and evaporatively cooled at a magnetic field controlled scattering length of $a_{\text{evap}} = -290 a_B$, where a_B is the Bohr radius. Next, we transported the atoms into a glass cell, where we used a further, vertically propagating optical dipole trap to locally enhance the density for a second efficient optical evaporation at a_{evap} . To reduce the vertical extension of the cloud, the atoms were transferred into a strongly elliptical dimple trap with a vertical waist of $w_z = 1.7 \mu\text{m}$. Two beams were shone in from the side, which interfered under a small angle to produce a vertical optical lattice of $3 \mu\text{m}$ spacing as illustrated in Fig. 1(a). The fermions loaded from the dimple trap populated mostly a single plane of this optical lattice. However, for high fidelity microscopy, almost all atoms in the adjacent planes need to be removed. This was achieved by transferring the atoms in undesired planes in a vertical magnetic field gradient from the $|1/2, \pm 1/2\rangle$ to the $|3/2, \mp 1/2\rangle$ states, which are subsequently lost due to spin changing collisions. The atoms in the final single plane were evaporatively cooled at a_{evap} , using a horizontal magnetic field gradient. The radial confinement counteracting this gradient was set independently by the depth of the vertical dipole trap. To produce a spin-polarized sample, we ramped the magnetic field to 27 G, where the magnetic moment of only the $|1/2, -1/2\rangle$ spin state vanishes. Then, we reduced the in-plane confinement until the gradient field completely removed the $|1/2, +1/2\rangle$ spin component, which we verified using Stern-Gerlach separation.

The optical lattice was tailored to the properties of ${}^6\text{Li}$, especially to its light mass m . In a lattice, the single particle energy scale is given by the recoil energy

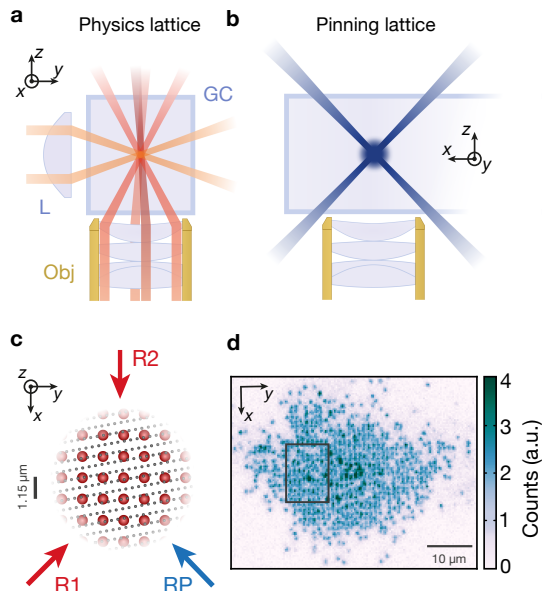


FIG. 1. **Experimental setup.** (a) Geometry of the physics lattice. A vertical standing wave of $3\ \mu\text{m}$ spacing is produced by focusing two beams with an aspheric lens (L) onto the atoms from the side. The horizontal lattice with a spacing of $1.15\ \mu\text{m}$ is formed by two pairs of beams focused through the imaging objective (Obj) beneath the glass cell (GC). (b) Pinning lattice beams viewed from the side. Two beams propagate close to the imaging objective in the x - z plane, while the third beam is in the y direction. All beams are retroreflected, forming a $532\ \text{nm}$ lattice. (c) Pinning lattice oversampling and Raman beam geometry viewed from top. For imaging, the atoms are loaded from the physics lattice (red dots) to the pinning lattice (gray dots). The Raman beams (red, R1 and R2) and repump beam (blue, RP) propagate in the x - y plane. For the pinning lattice, we show the sites within $\pm 250\ \text{nm}$ from one x - y plane of the physics lattice. In the experiment the relative position between pinning and physics lattice sites is not controlled. (d) Fluorescence image of $N = 763(10)$ ${}^6\text{Li}$ atoms acquired over 1 s of Raman sideband cooling. The black box marks the region where we evaluated the fluorescence statistics shown in Fig. 2.

$E_R = \hbar^2/8ma_l^2$, such that the lattice constant a_l can be large when the mass is small. For lithium, fast tunneling time scales in the kilohertz regime are realized even for $a_l > 1\ \mu\text{m}$. Thus, the strongly correlated regime is experimentally accessible, given the availability of Feshbach resonances to tune the interactions [23]. We loaded the atoms into such a large scale two-dimensional “physics” lattice with $a_l = 1.15\ \mu\text{m}$, produced by focusing phase coherent pairs of parallel beams with a custom microscope objective (numerical aperture 0.5, effective focal length $28\ \text{mm}$). The same objective was later used to collect the fluorescence signals during imaging [see Fig. 1(a)].

We used a deep additional “pinning” lattice with a lattice spacing of $532\ \text{nm}$ that oversampled the physics lattice [see Figs. 1(b), 1(c)] [24]. The $1064\ \text{nm}$ pinning lattice beams were retroreflected with waists of $56\ \mu\text{m}$ and an

average power of $22\ \text{W}$ per direction, resulting in an overall trap depth of $2.5\ \text{mK}$ and on-site trap frequencies of $1.3\ \text{MHz}$ on all axes. Prior to imaging, we transferred the atoms to the pinning lattice, which provides sufficient local confinement for Raman sideband cooling [25–27] with a Lamb-Dicke parameter $\eta \approx 0.23$. The Raman cooling (see supplemental material) was optimized for high fidelity imaging. The scattered photons provided the fluorescence signal [see Fig. 1(d)], which we detected with an electron-multiplied CCD camera [28, 29]. Over a detection period of 1 s, we collected on average 350 photons per atom, corresponding to a fluorescence rate of about $7\ \text{kHz}$. Parasitic background light was negligible during the 1 s exposure.

We reconstruct the physics lattice population via a local image analysis based on the point-spread function (PSF) of the detection system. We extract the PSF from fluorescence images of sparsely filled atomic samples by averaging many isolated single atom signals. This experimentally determined PSF is well approximated by a Gaussian with a standard deviation of $380(10)\ \text{nm}$, considerably larger than the specified and independently confirmed $290\ \text{nm}$. The first step of the reconstruction algorithm is to identify the position of the physics lattice on each single image by Fourier transforming the image and extracting the phase associated with the lattice wave vectors. The resulting physics lattice grid is shown in the inset of Fig. 2. Even though the atoms were held in the incommensurate pinning lattice during imaging, a clear

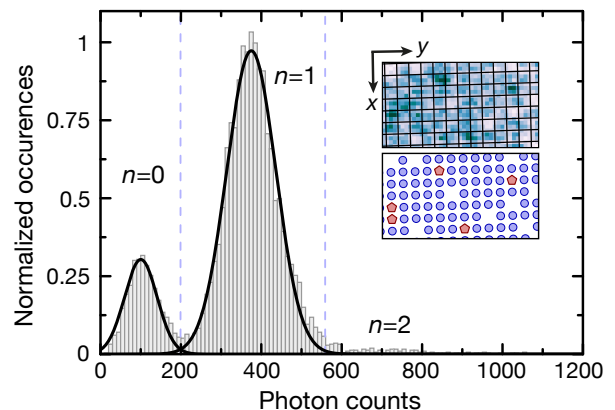


FIG. 2. **Lattice reconstruction.** Statistics of fluorescence levels obtained from the amplitude of local Gaussian fits per site. On 50 images, we evaluated the region marked in black in Fig. 1d with an average filling of 85%. The peaks in the histogram of $n = 0$ and $n = 1$ atoms are clearly separated (black lines are Gaussian fits). The few counts to the right are due to double occupancies (see supplemental information). The dashed lines mark the thresholds for identifying zero, one and two atoms per site. Inset: Close up of an exemplary fluorescence image with the results of the reconstruction shown below. Single atoms are marked with blue dots, red pentagons indicate double occupancies.

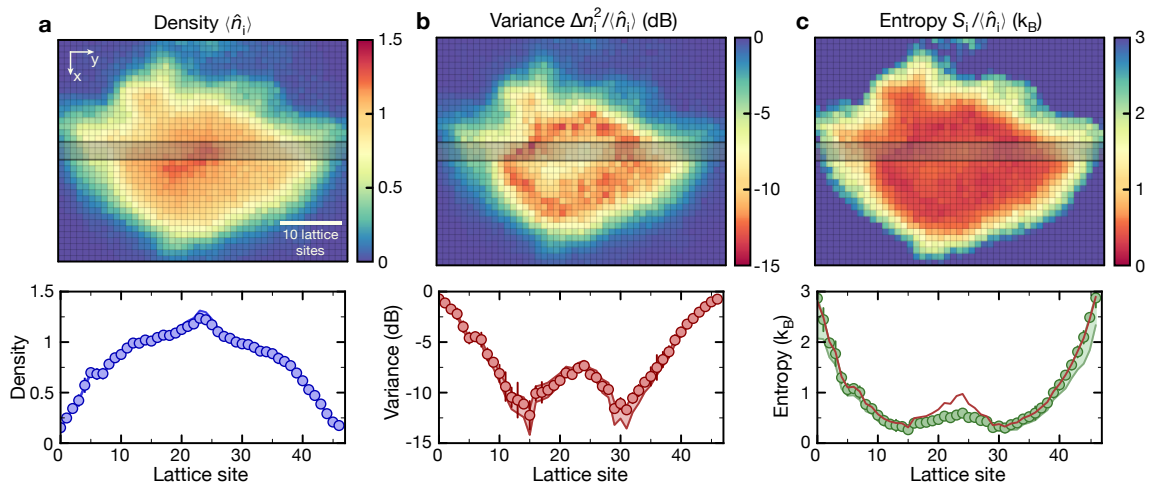


FIG. 3. **Local statistical analysis.** We analyze the local, single-site resolved occupation statistics of 425 images. Each pixel corresponds to a physics lattice site in the 2D histograms shown in the top row. Bottom row: horizontal cuts averaged over the vertical three sites indicated by the transparent box above. The shaded regions correspond to the systematic uncertainty in the local population assignment during reconstruction. Statistical error bars represent one standard deviation. **(a)** Average density. Pauli blocking results in a large region of approximately uniform density around the center. **(b)** Normalized atom number fluctuations. The band insulator manifests itself in the suppression of fluctuations most strongly in the region of approximately flat density in (a). In the wings of the cloud, Poissonian statistics is recovered. **(c)** Entropy per atom. The lowest entropies of $0.3 k_B$ are found in a ring around the center. The entropy increases towards the center and the edge due to the increase of double occupancies and holes, respectively. The red line is the result for the entropy, when assuming four instead of two accessible single particle states per site.

distinction of empty and singly occupied physics lattice sites is visible on the bare fluorescence image. Next, we determine the photon counts in each physics lattice site from a fit with the Gaussian approximated PSF. The resulting histogram of the fit amplitudes for images around unity filling [cf. Fig. 1(d)] per site is shown in Fig. 2. The peaks corresponding to empty and singly occupied sites are clearly distinct, resulting in a high fidelity of 99% for discriminating them. Furthermore, the histogram shows several events of high counts to the right of the $n = 1$ peak. We attribute these to doubly occupied physics lattice sites, which we identify with a reduced fidelity of $\simeq 70\%$ (see supplemental material). We expect to improve on the latter in future experiments, as the detection fidelity for double occupancies is at present mainly limited by our broadened PSF.

To estimate the influence of loss and hopping events, we took subsequent images of the same sparsely populated sample with 1 s exposure per image. We found a loss probability of 2.5(5)% and a tunneling probability of 5(1)% between two images averaged over a large detection region of $50 \times 50 \mu\text{m}$, where most of these events occur towards the edge of this region.

Next, we used the microscope to study the local statistics of spin-polarized, degenerate fermionic samples. After evaporation and spin polarization, we ramped up the physics lattice adiabatically within 100 ms to $8 E_R$. Before imaging, we rapidly increased the physics lattice depth to $20 E_R$ to freeze the atomic distribution. Then

we switched on the pinning lattice linearly within 5 ms. Setting the atom number between $N = 700$ and $N = 800$ fermions, we obtained images with high filling factors in the center of the trap [cf. Fig. 1(d)]. We took 425 images following this protocol and analyzed the local statistics of population for each lattice site. In the analysis, we took systematic errors due to the reconstruction as well as statistical uncertainties into account (see supplemental material).

The fermionic character of the gas is directly visible in the mean density $\langle \hat{n}_i \rangle$ per site i , shown in Fig. 3(a). In an inhomogeneously trapped sample, Pauli blocking leads to a plateau of unity filling. The overall shape of the cloud was determined by the trapping potential, which was not perfectly harmonic due to residual large-scale imperfections in our physics lattice beams. Even though the spin-polarized degenerate Fermi gas does not thermalize any more during lattice ramp up, our loading sequence resulted in a state close to a band insulator. Absence of thermalization hinders the redistribution of population from the first excited into the lowest band, which most likely limits the flatness of the observed density plateau. The atoms in the excited band accumulate in the trap center, where we detected an increased number of doubly occupied sites.

The incompressibility of the band insulator manifests itself locally as a suppression of on-site atom number fluctuations $\Delta n_i^2 = \langle \hat{n}_i^2 \rangle - \langle \hat{n}_i \rangle^2$ below the Poissonian variance given by $\langle \hat{n}_i \rangle$, expected for uncorrelated atoms.

Indeed, in the region of the density plateau we found strongly suppressed fluctuations with a normalized variance $\Delta n_i^2 / \langle \hat{n}_i \rangle = -11.9_{-2.7}^{+1.6}$ dB [see Fig. 3(b)], while the Poisson limit was recovered in the low density wings.

Enabled by the site resolved measurement of the lattice occupations and under reasonable assumptions on the accessible local quantum states, we reconstructed the local entropy S_i , without relying on a local density approximation or thermal equilibrium. The entropy per site $S_i/k_B = -\sum_E p_E^{(i)} \ln p_E^{(i)}$ was calculated from the occupation probabilities $p_E^{(i)}$ of all many-body energy eigenstates allowed for a given number of identical fermions distributed over k single particle states. Based on our observations, we limited the analysis to maximally two atoms per site. For non-interacting fermions, the probabilities p_E are directly related to the measured probabilities of finding zero, one or two atoms per site (see supplemental material). Here, we ignored the finite tunneling, which couples the different single particle states, leading to an overestimation of the inferred entropy. The number of populated single particle states was not directly accessible. Therefore, we analyzed the simplest case $k = 2$, and a second, maximal entropy scenario of $k = 4$, assuming the local ground state and three equally populated excited states, one per spatial direction. In Fig. 3(c), we present the resulting entropy distribution normalized to the mean site occupation. The two cases $k = 2$ and $k = 4$ converge in the limit of low double occupancy, showing that the entropy can be faithfully reconstructed in this regime. We extracted a minimum entropy per atom of $S_i / \langle n_i \rangle = 0.3(1) k_B$ in the density plateau region, while it increased towards the edge and the center, where the probability to find holes or two atoms was enhanced, respectively.

An upper limit to the temperature in the two-dimensional harmonic trap T_{ini} prior to lattice ramp-up can be deduced from the entropy measurement in the lattice. Based on the experimentally determined total entropy $\sum_i S_i = 1.05(5) N k_B$, we obtained $T_{\text{ini}}/T_F = 0.16(1)$, where T_F is the Fermi temperature [30, 31].

Our measurements described before reveal above unity filling in the center of the clouds. Contrary to earlier experiments [12, 14, 32], this observation indicates a suppression of parity projection, that is, the rapid loss of pairs of atoms in the same lattice site during fluorescence imaging. To set an upper bound on the probability for parity projection, we increased the density of the spin-polarized sample at constant atom number and measured the change in fluorescence and local site occupations. The density was controlled by the confinement in the initial harmonic trap, in which the gas was still in thermal equilibrium at chemical potential μ . When ramping up the optical lattice, the atomic sample cannot thermalize. Consequently, population above the energy E_R , around which the band gap opens, was transferred

into the first excited band. Hence, the filling factor in the center of the lattice increased with increasing μ . We indeed observed a compression of the cloud and a strong increase of the fluorescence level in the center of the cloud, but no measurable change in the total fluorescence signal [see Fig. 4(a)]. This provides strong evidence for a small probability of parity projection and that the photon scattering rate is constant, even when adjacent pinning lattice sites were filled – an important prerequisite for the detection of higher site occupations. In Fig. 4(b) we compare the fraction x_2 of doubly occupied to the fraction x_0 of empty sites. For the strongest compression, their values reach $x_2 = 0.3_{-0.05}^{+0.1}$ and $x_0 = 0.020(5)$, resulting in an upper limit to parity projection of 9%.

This observed suppression of parity projection is explained by the loading from the physics into the pinning lattice. Because of the shorter lattice constant of the pinning lattice, the number of states per Brillouin zone is increased compared to the physics lattice. When switching on the much deeper pinning lattice, states in the first ex-

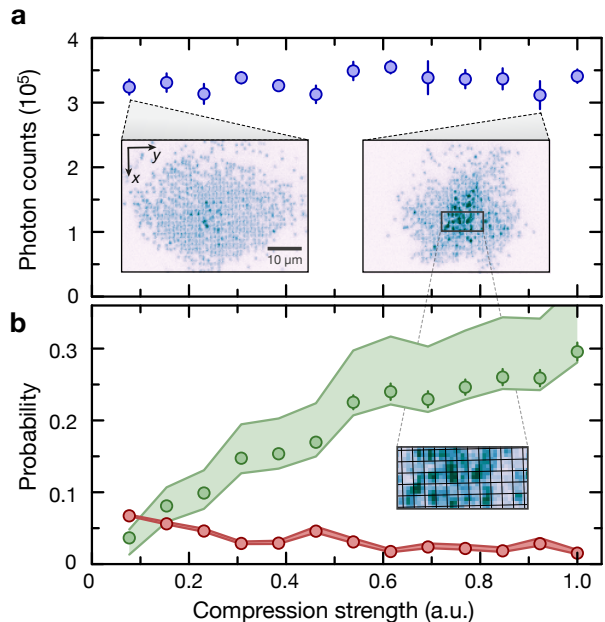


FIG. 4. **Absence of parity projection.** (a) Overall fluorescence level. We observe a constant total fluorescence level while increasing the density by trap compression. Insets: Representative images for two different compression strengths. Approximately unity filling is observed for weak compression, whereas for stronger confinement a dense core of multiply occupied sites is visible. (b) Probability of empty (red) and doubly (green) occupied sites versus compression strength. The number of holes decreases despite an increase in the number of doubly occupied sites. The shaded area corresponds to the systematic uncertainty in the local population assignment during reconstruction. Inset: Close-up of the central region marked by the black box in (a), demonstrating the localization of high fluorescence regions to individual lattice sites. Error bars are one standard deviation of the mean.

cited band of the physics lattice connect to states in the lowest band of the pinning lattice. Hence, initial double occupancies are separated into different pinning lattice sites as long as the switch on of the pinning lattice is adiabatic, which we ensured in our experiments.

In conclusion, we presented a site-resolved statistical study of single component degenerate fermionic lattice gases, directly demonstrating Pauli blocking in a textbooklike experiment. Additionally, we introduced a novel quantum gas microscope for fermionic ${}^6\text{Li}$, which separates the detection system from the physical system under study. Not only does it provide a way to circumvent parity projection, but it is also directly applicable to more advanced lattice geometries, such as superlattices. In the future, we expect it to give access to the local full counting statistics, even spin resolved. Combining such spin-resolved detection with local manipulation of the quantum gas [33] will enable a new generation of experiments with fermionic quantum matter that can range from the study of multipoint correlation functions [34], measurement of exotic quasiparticles and their dynamics [35] to advanced probing of nonequilibrium dynamics in many-body systems.

We thank S. Blatt and M. Greiner for helpful discussions and M. Lohse, T. Gantner, and T. Reimann for technical assistance while building the experimental setup. We acknowledge funding by the MPG and EU (UQUAM).

* ahmed.omran@mpq.mpg.de

- [1] A. G. Truscott, K. E. Strecker, W. I. McAlexander, G. B. Partridge, and R. G. Hulet, *Science* **291**, 2570 (2001).
- [2] T. Müller, B. Zimmermann, J. Meineke, J.-P. Brantut, T. Esslinger, and H. Moritz, *Phys. Rev. Lett.* **105**, 040401 (2010).
- [3] C. Sanner, E. J. Su, A. Keshet, R. Gommers, Y.-i. Shin, W. Huang, and W. Ketterle, *Phys. Rev. Lett.* **105**, 040402 (2010).
- [4] W. D. Oliver, J. Kim, R. C. Liu, and Y. Yamamoto, *Science* **284**, 299 (1999).
- [5] M. Henny, S. Oberholzer, C. Strunk, T. Heinzel, K. Ensslin, M. Holland, and C. Schönberger, *Science* **284**, 296 (1999).
- [6] H. Kiesel, A. Renz, and F. Hasselbach, *Nature (London)* **418**, 392 (2002).
- [7] M. Iannuzzi, A. Orecchini, F. Sacchetti, P. Facchi, and S. Pascazio, *Phys. Rev. Lett.* **96**, 080402 (2006).
- [8] T. Rom, T. Best, D. van Oosten, U. Schneider, S. Fölling, B. Paredes, and I. Bloch, *Nature (London)* **444**, 733 (2006).
- [9] T. Jelts, J. M. McNamara, W. Hogervorst, W. Vassen, V. Krachmalnicoff, M. Schellekens, A. Perrin, H. Chang, D. Boiron, A. Aspect, and C. I. Westbrook, *Nature (London)* **445**, 402 (2007).
- [10] N. Gemelke, X. Zhang, C.-L. Hung, and C. Chin, *Nature (London)* **460**, 995 (2009).
- [11] W. S. Bakr, A. Peng, M. E. Tai, R. Ma, J. Simon, J. I. Gillen, S. Fölling, L. Pollet, and M. Greiner, *Science* **329**, 547 (2010).
- [12] J. F. Sherson, C. Weitenberg, M. Endres, M. Cheneau, I. Bloch, and S. Kuhr, *Nature (London)* **467**, 68 (2010).
- [13] K. D. Nelson, X. Li, and D. S. Weiss, *Nat. Phys.* **3**, 556 (2007).
- [14] W. S. Bakr, J. I. Gillen, A. Peng, S. Fölling, and M. Greiner, *Nature (London)* **462**, 74 (2009).
- [15] M. F. Parsons, F. Huber, A. Mazurenko, C. S. Chiu, W. Setiawan, K. Wooley-Brown, S. Blatt, and M. Greiner, *Phys. Rev. Lett.* **114**, 213002 (2015).
- [16] E. Haller, J. Hudson, A. Kelly, D. A. Cotta, B. Peaudecerf, G. D. Bruce, and S. Kuhr, *Nat. Phys.* **11**, 738 (2015).
- [17] L. W. Cheuk, M. A. Nichols, M. Okan, T. Gersdorf, V. V. Ramasesh, W. S. Bakr, T. Lompe, and M. W. Zwierlein, *Phys. Rev. Lett.* **114**, 193001 (2015).
- [18] G. J. A. Edge, R. Anderson, D. Jervis, D. C. McKay, R. Day, S. Trotzky, and J. H. Thywissen, arXiv:1510.04744.
- [19] P. M. Preiss, R. Ma, M. E. Tai, J. Simon, and M. Greiner, *Phys. Rev. A* **91**, 041602 (2015).
- [20] T. Fukuhara, S. Hild, J. Zeiher, P. Schauß, I. Bloch, M. Endres, and C. Gross, *Phys. Rev. Lett.* **115**, 035302 (2015).
- [21] P. M. Duarte, R. A. Hart, J. M. Hitchcock, T. A. Corcovilos, T.-L. Yang, A. Reed, and R. G. Hulet, *Phys. Rev. A* **84**, 061406 (2011).
- [22] J. Sebastian, C. Gross, K. Li, H. C. J. Gan, W. Li, and K. Dieckmann, *Phys. Rev. A* **90**, 033417 (2014).
- [23] C. Chin, R. Grimm, P. Julienne, and E. Tiesinga, *Rev. Mod. Phys.* **82**, 1225 (2010).
- [24] M. D. Shotton, *Phys. Rev. A* **83**, 033617 (2011).
- [25] C. Monroe, D. M. Meekhof, B. E. King, S. R. Jefferts, W. M. Itano, D. J. Wineland, and P. Gould, *Phys. Rev. Lett.* **75**, 4011 (1995).
- [26] S. E. Hamann, D. L. Haycock, G. Klose, P. H. Pax, I. H. Deutsch, and P. S. Jessen, *Phys. Rev. Lett.* **80**, 4149 (1998).
- [27] A. J. Kerman, V. Vuletić, C. Chin, and S. Chu, *Phys. Rev. Lett.* **84**, 439 (2000).
- [28] Y. S. Patil, S. Chakram, L. M. Aycock, and M. Vengalattore, *Phys. Rev. A* **90**, 033422 (2014).
- [29] B. J. Lester, A. M. Kaufman, and C. A. Regal, *Phys. Rev. A* **90**, 011804 (2014).
- [30] L. D. Carr, G. V. Shlyapnikov, and Y. Castin, *Phys. Rev. Lett.* **92**, 150404 (2004).
- [31] Y. Castin, in *Ultra-cold Fermi Gases*, edited by M. Inguscio, W. Ketterle, and C. Salomon (2007).
- [32] M. T. DePue, C. McCormick, S. L. Winoto, S. Oliver, and D. S. Weiss, *Phys. Rev. Lett.* **82**, 2262 (1999).
- [33] C. Weitenberg, M. Endres, J. F. Sherson, M. Cheneau, P. Schauß, T. Fukuhara, I. Bloch, and S. Kuhr, *Nature (London)* **471**, 319 (2011).
- [34] M. Endres, M. Cheneau, T. Fukuhara, C. Weitenberg, P. Schauß, C. Gross, L. Mazza, M. C. Bañuls, L. Pollet, I. Bloch, and S. Kuhr, *Science* **334**, 200 (2011).
- [35] M. Cheneau, P. Barmettler, D. Poletti, M. Endres, P. Schauß, T. Fukuhara, C. Gross, I. Bloch, C. Kollath, and S. Kuhr, *Nature (London)* **481**, 484 (2012).
- [36] M. S. Safronova, U. I. Safronova, and C. W. Clark, *Phys. Rev. A* **86**, 042505 (2012).

SUPPLEMENTAL MATERIAL

Atomic sample preparation

Our experiments started in a standard magneto-optical trap (MOT) of ${}^6\text{Li}$ at 671 nm in a steel octagon vacuum chamber, which was loaded from a Zeeman slower in 4 s. We then illuminated the cloud with MOT beams at 323 nm, driving the $2S_{1/2} \rightarrow 3P_{3/2}$ transition, which has an effective linewidth of $2\pi \times 750$ kHz, 8 times lower than the principal transition at 671 nm and a correspondingly lower Doppler temperature [21, 22]. The ultraviolet (UV) MOT requires two frequencies, one for cooling and one for repumping out of the $F = 1/2$ ground state. After a 12 ms UV cooling stage, the atoms reached a temperature of $70 \mu\text{K}$, which facilitates direct optical trap loading. During the UV MOT, we ramped up a large volume single beam optical “collection” dipole trap, derived from a high power, broadband 1070 nm laser. The collection trap had a power of 65 W and a waist of $100 \mu\text{m}$ at the position of the atoms and a wavelength close to the magic one of the UV transition, where the differential light shift vanishes [36]. We extinguished the UV repumping beam before the cooling beam to optically pump the atoms into an incoherent spin mixture of the $F = 1/2$ sublevels. We evaporatively cooled the atoms in the collection trap at a background magnetic field of 320 G, which sets a scattering length of $-290 a_B$ between the two spin components. The magnetic field had a curvature confining the atoms along the axial direction of the trap. At the end of the 5 s linear evaporation ramp, we transferred the atoms into a tightly focused optical “transport” trap at 1064 nm ($P = 3.5$ W, $w_0 = 30 \mu\text{m}$). Its focus was shifted by movable optics on an air bearing translation stage over 28 cm in 0.5 s, transporting the atoms into a glass cell for better optical access. After this transport, the typically 10^6 atoms had a temperature of $13 \mu\text{K}$.

We then ramped up a magnetic field of 320 G and a vertical optical “cross” trap of 3 W power and $w_0 = 110 \mu\text{m}$ that intersected the transport trap under an angle of 100° , and applied forced evaporation in this crossed dipole trap for 3 s. A strongly elliptical dimple trap at 780 nm with $w_x = 10.3 \mu\text{m}$ and $w_z = 1.7 \mu\text{m}$ captured up to 10^4 atoms from the crossed trap and confined them vertically. Subsequently, we ramped up the vertical lattice beams, which are derived from a single frequency 1064 nm Yb fiber amplifier. They were focused onto the atoms with a waist of $w_0 = 150 \mu\text{m}$ and intersected under an angle of 40° to generate a standing wave of $3 \mu\text{m}$ spacing and distribute the atoms mainly along a single plane. As the confinement along the lattice beam direction was very weak, the vertical cross trap was kept on during this time to give the atoms additional radial confinement in the plane. Since single plane loading from the dimple trap did not work with unity fidelity, we need to

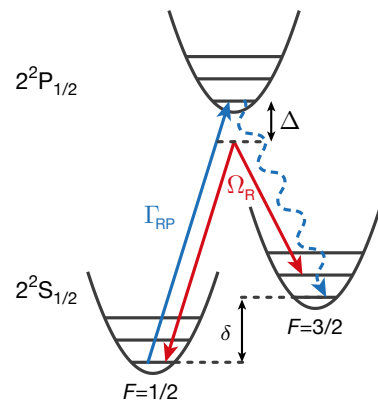


FIG. S1. **Raman sideband cooling scheme.** Two Raman beams, each red detuned by $\Delta = 7.3$ GHz to the D_1 line, provide the coupling Ω_R between different vibrational levels $|F = 3/2, \nu\rangle \Leftrightarrow |F = 1/2, \nu - 1\rangle$. A repump beam (blue) optically pumps the atoms from the $|F = 1/2, \nu - 1\rangle$ into the $|F = 3/2, \nu - 1\rangle$ state with a scattering rate Γ_{RP} . The hyperfine levels are split by $\delta = 228.2$ MHz and the frequency difference between the lowest vibrational levels is 1.3 MHz.

remove atoms from adjacent planes. We applied a vertical magnetic field gradient of 18 G/cm at a bias field of 14.6 G and used radio frequency transitions to locally transfer the atoms from $|1/2, \pm 1/2\rangle$ to the $|3/2, \mp 1/2\rangle$ states. These are unstable with respect to spin changing collisions and we confirmed their loss from the spin flipped planes by radio frequency spectroscopy.

For final evaporative cooling, we ramped up a magnetic bias field of 320 G pointing along a direction in the plane and slowly increased a magnetic field gradient along the same direction up to 15 G/cm in 2 s. The two spin components experience almost the same magnetic force as their magnetic moment is nearly equal at this offset field. Therefore, we maintained a balanced and thermalized spin mixture at the end of the final evaporation.

The horizontal physics lattice was generated by pairs of parallel beams derived from a 1064 nm Nd:YAG laser. They were focused through the high resolution microscope objective onto the atoms to waists of $180 \mu\text{m}$. All beam pairs of the 3D physics lattice had different frequencies to avoid cross-interference between different lattice axes. The lattice beams were slowly ramped on after the last evaporative cooling stage, setting the starting point of all further experiments.

Imaging via resolved Raman sideband cooling

We used resolved Raman sideband cooling [25–27] in the pinning lattice to image the atoms. For our configuration, shown in Fig. S1, the Lamb-Dicke parameter is $\eta \approx 0.23$, sufficient to suppress the transfer of

atoms to different bands during scattering. The atoms were continuously illuminated with two linearly polarized Raman beams at a relative angle of 135° and a common red-detuning of $\Delta = 7.3$ GHz with respect to the D_1 line. Their relative detuning was set to couple the $|F = 3/2, \nu\rangle$ and $|F = 1/2, \nu - 1\rangle$ states, where ν denotes the vibrational quantum number. The magnetic field was small (below 10 mG), hence all underlying hyperfine sublevels were degenerate. The Raman beam orientation was chosen such that the total Raman momentum transfer $\Delta\vec{k}$ had an equal projection on all pinning lattice axes. This provides an equal effective coupling strength of $\Omega_R \approx 2\pi \times 90$ kHz on the red sidebands. To expand the spatial cooling region and to couple higher onsite vibrational levels in the anharmonic regime, we also modulated the two-photon detuning sinusoidally to address on-site trap frequencies between 900 kHz and 1.3 MHz. The circularly polarized repump light entered orthogonally to the first Raman beam in the same plane and was 3Γ blue detuned from the bare atomic transition $|2S_{1/2}, F = 1/2\rangle \rightarrow |2P_{1/2}, F = 3/2\rangle$, where $\Gamma = 2\pi \times 5.8$ MHz is the natural width of the upper state. This detuning compensated for the differential light shift in the pinning lattice. In this configuration, the atoms were optically pumped into the $|F = 3/2, \nu = 0\rangle$ state, which only couples to the Raman and repump light via off-resonant scattering.

Reconstruction in regions of high filling

In regions of low and moderate filling (up to approximately unity density per site), the discrimination between zero and one atom per site can be done with 99% fidelity (cf. main text Fig. 2). The situation becomes more challenging for higher filling as can be seen in Fig. S2, where we compare histograms extracted from different local regions. Instead of a clear peak for $n = 0$, the high density histogram shows a tail at low counts. The leakage of the signal due to empty sites into the $n = 1$ region, determined after subtraction of the Gaussian fitted single occupation peak, results in an underestimation of the holes by up to 20%.

The main challenge lies in the discrimination between occupations of $n = 1$ and $n = 2$. The high density histogram shown in Fig. S2 displays a long tail to the right instead of a well defined maximum around twice the single atom count rate. This causes difficulties when determining an accurate threshold between $n = 1$ and $n = 2$. We set this threshold such that the mean count rate of single atoms is in the center of the $n = 1$ region. While there is a significant amount of signal well above this threshold, there are many occurrences around the threshold value. This is the main source for systematic errors in determining the correct occupation number for these photon counts.

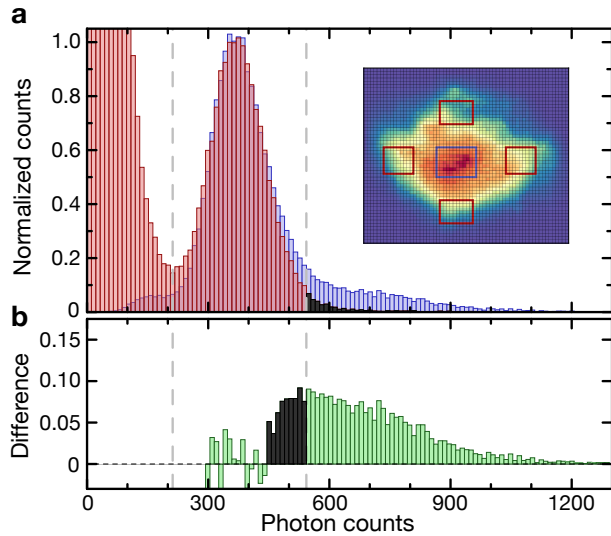


FIG. S2. **Comparison of reconstructed photon counts in regions of high and moderate density.** The dashed lines correspond to the thresholds discriminating the different occupation numbers. **(a)** Histograms of the amplitude of the local Gaussian PSF fits for the center of the cloud (blue) and the edges of cloud (red) normalized to match around and to the left of the $n = 1$ peak. The black region indicates wrongly assigned double occupancies. The regions used to extract the histogram are indicated in the inset. Compared to the histogram shown in Fig. 2 of the main text, the signal from empty sites in the dense center (left part of the blue histogram) shifts to the right. Also, the separation of the zero and one peaks in the red moderate filling histogram is slightly reduced. This is due to inhomogeneities in the photon count rate across the cloud of approximately 10% and due to the increased hopping and loss around the cloud edges. **(b)** Difference between both histograms in the region of high counts. The black area marks wrongly assigned single occupancies.

To estimate these errors, we compare the histogram extracted from the central high density region to the ones of moderate density regions along the edge of the cloud. We find a clear difference for higher photon counts between them (see Fig. S2). For the comparison, we normalized the histograms to each other, such that they overlap around the center and left slope of the $n = 1$ peak. Then, we subtracted both histograms to get a residual signal that we attribute to the double occupancies. Of these residual counts, the events below the threshold are interpreted as double occupancies that are falsely assigned as single atoms. This region has an area which is around 30% of the area above the threshold, therefore our measured number of double occupancies is underestimated by up to this percentage. We also analyzed the signal from the single atoms at the edge of the system that resulted in a few events exceeding the threshold. These constitute around 2.5% of the total single atom signal and represent single atoms falsely identified as double occupancies.

Furthermore, each wrong assignment of a doubly occupied site results in the opposite wrong assignment of a single occupancy. We took these anti-correlated systematic errors in the probabilities for single and double occupancies into account when analyzing the uncertainty of the local mean, number fluctuations and entropy. These systematic uncertainties are given by the shaded areas in our plots in the main text.

Entropy analysis

Given the measurement of the local occupation probabilities, we extracted the entropy per site S (we drop the site index for better readability). Our analysis is based on the many-body states (with occupation probabilities p_E) of up to two fermions on k single particle levels with occupation probabilities y_i . The corresponding entropy per site is then given by $S/k_B = \sum_E p_E \ln p_E$. In the main text we present the results for $k = 2$, for which the population of the local energy eigenstates are

$$\begin{aligned} p_0 &= (1 - y_0)(1 - y_1) = x_0 \\ p_1 &= y_0(1 - y_1) \\ p_2 &= y_1(1 - y_0) \\ p_3 &= y_0 y_1 = x_2. \end{aligned}$$

Here, p_0 and p_3 are the probabilities for zero and two fermions, corresponding to the lowest and highest energy eigenstate. The probabilities for the remaining two eigenstates are p_1 and p_2 and describe a single fermion in the lower and upper single particle level, respectively. All p_E can be calculated from the measured probabilities for holes and double occupancies, x_0 and x_2 respectively. We extended the analysis in the same spirit to the case $k = 4$, assuming an equal population of the three upper single particle levels. These upper levels correspond to the first excited states of the local three dimensional harmonic oscillator. This gives a reasonable upper bound for the inferred entropy. In regions of low double occupancy, this has a minor effect on the detected entropy, leading to an increase from $0.3 k_B$ to $0.34 k_B$ of the minimal measured entropy per particle. In the center of the cloud, where the fraction of double occupancies is higher, the inferred entropy increases from $0.6 k_B$ to $0.95 k_B$.